Fatigue crack growth in compacted and spheroidal graphite cast irons

Jérôme Hosdez, N. Limodin, Denis Najjar, Jean-François Witz, E. Charkaluk, Pierre Osmond, Agathe Forre, F. Szmytka

Fatigue crack growth in compacted and spheroidal graphite cast irons

J. Hosdez[a], N. Limodin[a], D. Najjar[a], J-F. Witz[a], E. Charkaluk[b], P. Osmond[c], A. Forré[d], F. Szmytka[e]

[a] *Univ. Lille, CNRS, Centrale Lille, Laboratoire de Mécanique, Multiphysique et Multiéchelle (LaMcube) FRE 2016, 59000 Lille, France.*
[b] *Laboratoire de Mécanique des Solides (LMS), UMR CNRS 7649, 91762 Palaiseau, France.*
[c] *Chassis and Engine Material Department, Groupe PSA, 78955 Carrieres sous Poissy, France.*
[d] *Science and Future Technologies Department, Groupe PSA, 78140 Vélizy-Villacoublay, France.*
[e] *Institut des Sciences de la Mécanique et Applications Industrielles (IMSIA), UMR EDF/CNRS/CEA/ENSTA 9216, 91762 Palaiseau, France.*

Abstract

The present paper focuses on the fatigue life of a Compacted Graphite cast Iron (CGI) as compared to a Spheroidal Graphite cast Iron (SGI). Fatigue crack growth laws have been determined with digital image correlation. Main difference between the materials is that cracks propagate faster in the CGI than in the SGI. X-ray tomography was also used in order to assess graphite morphologies and crack shapes. A complex morphology was observed for the vermicular graphite with rounded edges that limit notch effects. The crack spreads easily in CGI via a quasi cleavage mechanism and by propagating through graphite mainly by breaking the vermicules.

Keywords: Compacted Graphite cast iron, Spheroidal graphite cast iron, Microtomography, Fatigue, Crack propagation

1. Introduction

Graphite cast irons are used in a large number of applications subjected to mechanical fatigue due to cost effectiveness and good strength. They are regularly used in the automotive industry [1, 2] especially for exhaust systems as they have good mechanical characteristics at high temperature. Graphite

cast irons present graphite inclusions and a ferritic and/or pearlitic matrix. A wide variety of structures of the graphene sheets can be generated leading to the formation of different graphite shapes by adjusting cooling rates and the concentration of alloying elements.

Graphite cast irons are classified from the morphology of the graphite inclusions such as Spheroidal, nodular or ductile Graphite Iron (SGI), Flake or lamellar Graphite Iron (FGI) and Compacted or vermicular Graphite Iron (CGI). For spheroidal graphite cast Iron, Miao *et al.* [3] and Llorca *et al.* [4] showed that graphite grows radially to form spheroids either with limited connection between neighbouring nodules, or even completely isolated, leading to a high mechanical resistance and toughness [5]. Flake Graphite cast Irons contain connected graphite particles which tend to grow in covalent bonds plane and are thus anisotropic. The main characteristic of flake graphite is the high level of connectivity of lamellae in three-dimensions that leads to a better thermal conductivity than SGI, but offers less attractive mechanical properties especially in the fatigue field [6] except for braking applications [7]. The compacted graphite cast iron presents vermicular graphite particles that look like corals with large, thin and rounded branches. Llorca *et al.* [4] and Tartera *et al.* [8] assumed that compacted graphite nucleates as spheroid and develops later branches with rounded ends. Its mechanical properties are intermediate between the previous two cast irons [6] with a thermal conductivity which is better than for SGI [9].

The ability to characterize shape of graphite inclusions was the emphasis of several studies [10, 11]. Indeed, reproducible quantitative analysis of the microstructure of cast iron helps to understand the correlation between the shape of graphite and materials properties. Graphite particles shape may greatly influence the thermal response of the cast iron. Indeed, the thermal conductivity of graphite in grey cast iron is three to five times superior to that of the ferrite matrix [12]. A graphite impact on the mechanical properties is observed for cast irons [13, 14, 15]. For example, the graphite size has an influence on fatigue

strength [16] as the largest irregularly shaped nodules reduce both this latter and fracture toughness. The specific shape of the graphite in the metal matrix can also act as a crack shield and lower the stress intensity factor close to the crack tip. This is especially the case for SGI which constitutes an appropriate material for cyclically loaded structures [17, 18, 19] (and also in some cases FGI with brake discs for example [7]). Moreover, some studies highlighted crack closure effects especially in ductile cast iron [20]. The crack damages spheroids during its progress by shearing the nodules poles conducting to a blunting effect [21]. On the contrary, flake graphite is similar to a notch and leads to stress concentration in the metallic matrix so that cracks easily propagate over a length equal to the flake size after interface debonding. For graphite inclusions, size, shape and distribution have no significant influence on cyclic hardening of the material but they play a great role in the crack initiation and propagation process [6]. Therefore, in order to prevent catastrophic failures and to lengthen the service lifetime of structures, it is of primary importance to consider the influence of the graphite geometrical features on the fatigue crack initiation and propagation. Mechanical properties of grey cast iron are also determined by the metal matrix. A pearlitic matrix exhibits high strength and hardness and is prone to a brittle fracture, while a ferritic cast iron is rather ductile and soft [22]. A matrix with both ferritic and pearlitic phases conducting to intermediate mechanical properties is often found in practice. Thus, cast irons properties (except inelastic behaviour) are predominantly controlled by the shape of the graphite particles in combination with the matrix constituents. Due to its balance between mechanical and thermal properties, compacted graphite cast iron is more and more employed for applications involving thermomechanical fatigue. Although CGI has been discovered for more than forty years and despite a few papers have been published [23, 24, 25, 26], its properties are not well known yet.

Finally, more research is needed for a better understanding of the mechanical behaviour of the compacted graphite cast iron SiMoNi for which only limited experimental data are available on the fatigue crack growth behaviour. This

manuscript presents therefore an experimental study of fatigue behaviour of CGI with an analysis of graphite shape. As the graphite is dispersed through the volume of the casting, in a 3D distribution, X-ray tomography is required to determine the 3D morphology of the graphite without any shape assumptions. Results are compared with those of a SGI, commonly used for applications related to mechanical fatigue. In the first part, studied cast irons are presented as well as the different methods employed, i.e. X-ray microtomography and its analysis methodology and mechanical tests. In the second part, results of 3D characterization by tomography and mechanical tests are shown and discussed. The final section presents the main conclusions and possible future works.

2. Materials and methods

2.1. Materials presentation

2.1.1. Compositions

Two cast irons are studied in this work: a Spheroidal Graphite cast Iron (SGI) and a Compacted Graphite cast Iron (CGI). Materials were supplied in the form of foundry bars, obtained by gravity die casting, with a length of 200 mm and a diameter of 25 mm. Their chemical compositions are specified in Table 1.

	C	**Si**	**Mo**	**Mn**	**Ni**	**P**
SGI	3.4	3.89	0.57	0.15	0.019	0.025
CGI	3.4	5	0.8	3	0.7	0.07

Table 1: Chemical compositions of the studied cast irons (weight %).

One noticeable difference between CGI and SGI compositions is the silicon content with respectively 3.89 and 5%. All graphitic cast irons contain relatively high concentrations of Si, which enhances graphitization. The addition of silicon also improves the strength of the ferritic matrix by solid solution strengthening effect and grain size reduction. Moreover, it confers a good heat resistance by

improving microstructural stability, i.e. by increasing the allotropic transformation temperature and oxidation resistance [27]. Higher nickel and manganese contents are also to be reported for the CGI due to heat resistance and pearlite formation considerations respectively. Both graphite cast irons were developed with the aim to design structures working at high temperature such as exhaust manifolds.

2.1.2. Overview of microstructures

Metallographic samples were prepared according to standard procedures and examined by microscopy. Optical and electronic microscopies were employed to observe the microstructures of cast irons samples. Typical micrographs from Scanning Electron Microscopy (SEM) illustrating the microstructure of the materials are shown in Fig. 1 (a,b).

The 2D images obtained using SEM are analysed via ImageJ software. Microstructures present mostly graphite under the form of nodules or vermicules surrounded by a ferritic matrix. Both graphite cast irons contain less than 5% of lamellar pearlite at grain boundaries and show a homogeneous distribution of graphite. In SGI, graphite nodules are globally spheroidal with a mean diameter that is close to 25 μm and in some instances reaches up to 45 μm (Fig. 2 (a)). In the compacted graphite cast iron, the vermicule shape might be described as coral-like, or 'worm-shaped'. It is long, relatively flat and slender with rounded branches having a typical length close to 50/60 μm and a thickness of 10 μm (Fig. 1 (b)). Thus, compacted graphite elements are elongated and randomly oriented in the ferritic matrix. Moreover, in the CGI, some graphite nodules subsist (Fig. 2 (b)).

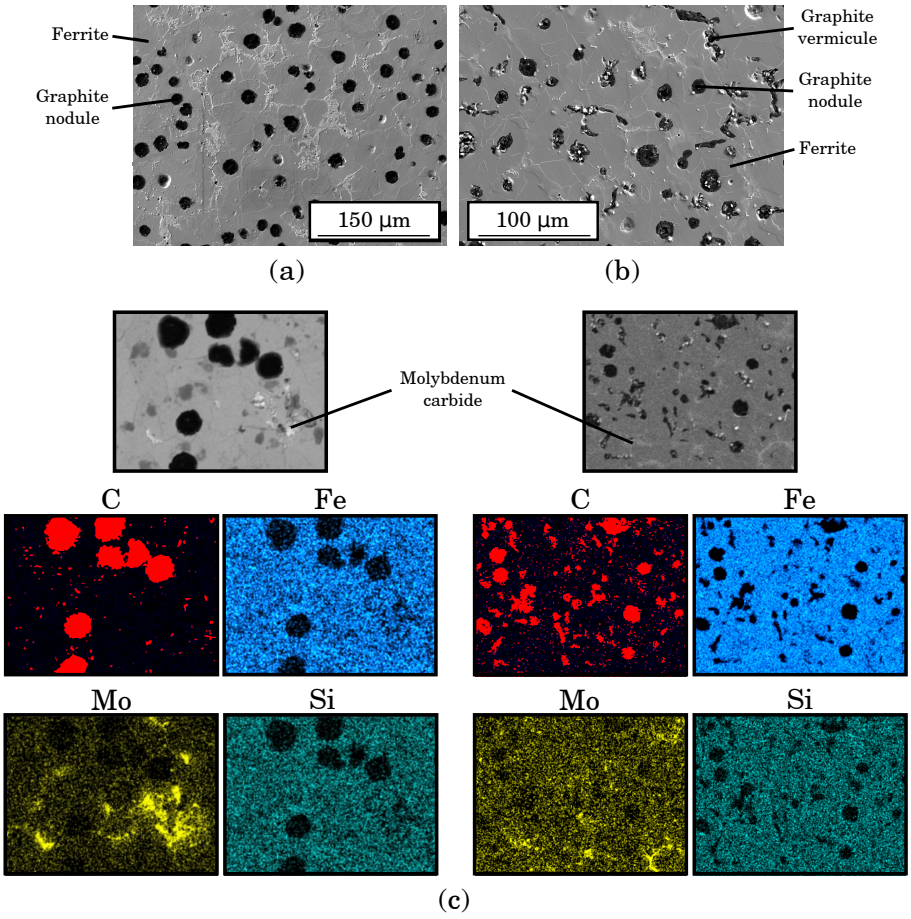

Figure 1: Spheroidal (a) and compacted (b) graphite cast irons microstructures observed with SEM. EDX maps (c) of chemical elements included in SGI (left) and CGI (right).

115 An Energy Dispersive X-ray Spectroscopy (EDX) analysis was also performed on sections of both types of cast irons (Fig. 1 (c)). A high level of molybdenum is highlighted for each material at grain boundaries and corresponds to molybdenum carbides, which confer good mechanical resistance at high temperature, but could conduct to material brittleness [27].

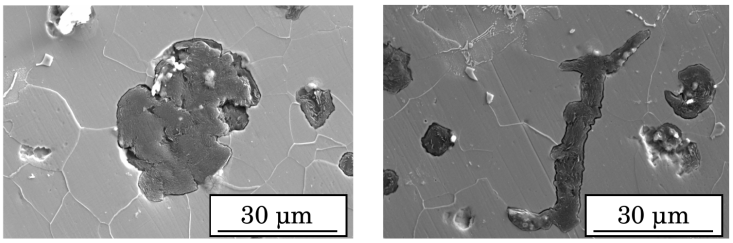

Figure 2: Zoom on graphite nodule (a) and vermicule (b) observed with SEM in topographic contrast.

Nonetheless, graphite particles are difficult to characterize in microscopy as graphite morphology is highly three-dimensional. Indeed, although a vermicular graphite is a flake in 2D (Fig. 2 (b)), it actually belongs to a 3D coral network. To go further in graphite characterization, X-ray microtomography is necessary.

2.2. Microtomography characterization

2.2.1. Test conditions

Laboratory X-ray micro-tomography was conducted at the *In Situ* Innovative Set-ups under X-ray micro-tomography (ISIS4D) platform [28]. The micro-tomography experiments were performed using a computed tomography system Ultra Tom from RX solutions. A nano-focus tube was employed with a 100 kV acceleration voltage and a filament current of 65 μA. Specimens were placed on the rotating stage between the X-ray source and a flat panel detector of 1874x1496 pixels. A set of 1440 radiographs were taken while the sample was rotated through 360° along its vertical axis. Six images were averaged at a given angular position to reduced noise. Reconstruction of the tomographic data is performed with a filtered back-projection algorithm [29] using X-Act software.

Cubic samples for micro-tomography were extracted from the middle of the foundry bars with a micro-cutting machine to limit material damage. They were small enough, i.e. around 2x2x2 mm^3, in order to ensure a high resolution of tomography. Indeed, specimens with a diagonal less than 3 mm are required for

X-ray tomography observations at a voxel size (~ 1.75 μm) suitable for graphite characterization.

2.2.2. Analysis methodology

Characterization of graphite through 3D image analysis was performed using Avizo [30] and ImageJ [31] softwares. The methodology can be summarized as follows (Fig. 3):

- A ROI (Region Of Interest) of 0.7 mm^3 was defined in order to limit the size of reconstructed data and ensure a same analysis volume for both samples (Fig. 3 (a)).
- A median and an anisotropic diffusion filters were employed to reduce image noise (Fig. 3 (b)).
- Graphite segmentation was achieved with a simple threshold of grey levels, i.e. by selecting minimum and maximum values for the studied phase (Fig. 3 (c)).
- Connected voxels of thresholded graphite particles were determined and labelled with Avizo (Fig. 3 (d)). The object labelling step allows to assign every connected object in the binarized image a unique label for each object. Then, these labelled objects were analyzed separately.
- Elements located on the boundaries of the ROI were also neglected for the morphological analysis but kept for volume fraction computations. All boundaries of the labelled regions were smoothed before surfaces generations (Fig. 3 (e)).

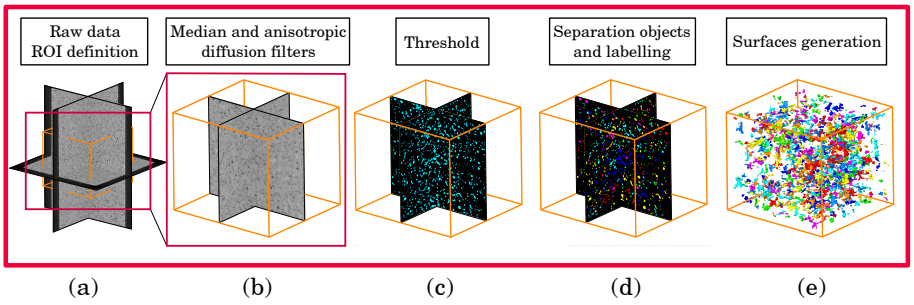

Figure 3: Main steps of the generation of labelled elements for graphite analysis (with a cubic ROI having an edge of 885 μm size).

A quantitative analysis was performed on independent, i.e. labelled, elements of graphite. Herein, the main shape factors retained are sphericity, equivalent and Feret diameters:

- The sphericity was introduced, according to Equation 1, in Avizo quantification tools in order to differentiate segmented graphite by their shape, i.e. nodules and vermicules. Sphericity varies between zero and one with the maximum value corresponding to a perfect spherical shape and the minimum corresponding to a particle with high anisotropy.

$$F = 6\sqrt{\pi}\frac{\text{Volume}}{\sqrt{\text{Area}^3}} \tag{1}$$

- The equivalent diameter (Eq. 2) in three dimensions is the diameter of a sphere that would have the same volume as the studied object.

$$D_{eq} = 2\left(\frac{3\text{Volume}}{4\pi}\right)^{1/3} \tag{2}$$

- The maximum Feret diameter (the minimum Feret respectively) is the distance between the two most distant points (respectively the closest) on the object's borders.

2.3. Mechanical test

Microstructures and particularly graphite particles influence the mechanical behaviour of each grey cast iron. Tensile and micro/macro Vickers hardness tests were conducted in order to evaluate some trends before focusing on fatigue behaviours.

2.3.1. Hardness and tensile tests

Micro and macro hardness tests were performed for both spheroidal and vermicular graphite cast irons. Samples were extracted at the heart of the foundry bars and about twenty measurements were achieved per material. The applied loads were 30 kilograms for macro-hardness and 100 grams for micro-hardness tests.

Monotonic tensile tests allowed to determine the main mechanical characteristics of the cast irons. Quasi-static tensile tests were carried out at a constant speed of 0.5 mm/min with Instron tensile test equipment with a 25 kN load-cell. Standard dog bone specimens were cut by electro-discharge machining and polished (Fig. 4 (a)). The strain was measured continuously with a digital video extensometer during the test.

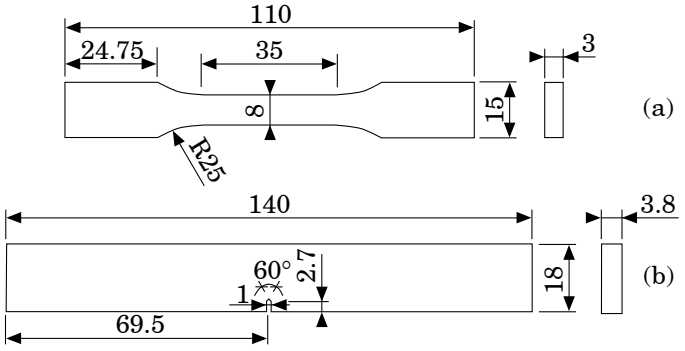

Figure 4: Specimens geometry for tensile (a) and fatigue tests based on ASTM E647 (b).

2.3.2. Fatigue crack growth tests

A Single Edge Notch Tension (SENT) test piece (based on ASTM E647), with a length of 140 mm, a thickness of 3.8 mm and a width of 18 mm was cut from the cast bars (Fig. 4 (b)). A straight-through notch with an opening angle of 60° at the notch tip, with a total length of 3.4 mm and a height of 1 mm was cut by electro discharge machining. The specimen was fatigue tested under mode I loading until failure. A pre-cracking step with a load shedding procedure [32] was performed to grow a long sharp fatigue crack in small scale yielding conditions (Fig. 5). During this step, the load was progressively decreased to limit the stress intensity factor increase with the crack growth using a Direct Current Potential Drop (DCPD) method described in [33]. Specimens were observed with a camera triggered to the load-cell of the fatigue machine. Pictures were taken every 50 cycles at the maximum and the minimum load values. The camera was equipped with a telecentric lens to avoid distortions, false perspectives and to attain a pixel size of 5.25 μm with a definition of 2048 by 2048 pixels. Displacement fields were determined by using Digital Image Correlation (DIC) technique. To ensure a good spatial resolution, the DIC procedure was achieved with 4x4 pixels windows by means of a paint speckle pattern that was sprayed by an air-brush.

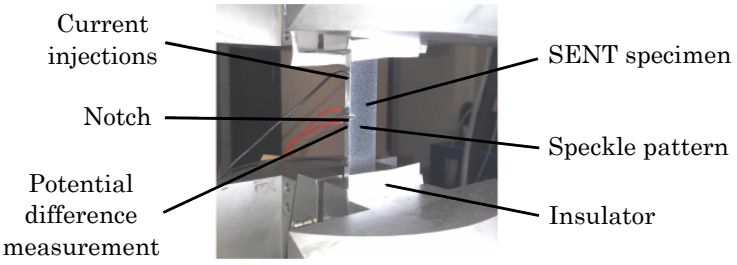

Figure 5: SENT specimen with a speckle pattern for DIC and inputs/outputs for DCPD method.

At a load ratio of 0.1 and a constant maximum stress intensity factor K_{Imax} of 12 MPa$\sqrt{\text{m}}$ (10 MPa$\sqrt{\text{m}}$) for SGI (for CGI respectively), a one millimeter

long pre-crack was produced. Then, a sinusoidal loading profile was applied with constant maximum values of 6.8 kN and 6 kN for SGI and CGI respectively during the propagation step; compacted graphite cast iron was cycled at smaller loads assuming a weaker fatigue crack growth resistance. The selected loads allowed to begin with SIFs close to the thresholds of cast irons [6]. The load ratio and the frequency were 0.1 and 2 Hz respectively.

2.3.3. Experimental and numerical mechanical fields

A projective digital image correlation method was used to identify Paris' crack propagation laws. The DIC procedure was performed using YaDICs programming platform, developed in the LaMcube laboratory [34]. The retained DIC methodology is based on a local approach with a non-continuous description. The projection is carried out on the Williams' model which expresses displacements in a cracked medium in the small scale yielding conditions [35, 36, 33] under the form of expansion series [37]. More details about the projection method can be found in [33]. It can be summarized as follows:

- The displacement gradient in the loading direction is computed from DIC measurements and thresholded to detect the crack tip location.
- As the crack length is acquired, the analytical expression of Williams can be constructed.
- The SIFs ranges ΔK_I and ΔK_{II} are computed by a minimization of the difference between experimental and analytical fields via a least squares method.

3. Results and discussion

3.1. Microtomography analysis

To further understand the differences in mechanical properties between spheroidal and compacted graphite cast irons, a graphite morphology analysis was carried out with microtomography.

3.1.1. Sphericity characterizations

In SGI, graphite appears as non-interconnected particles with a sphericity above 0.60 and a bi-modal repartition: the predominant mode is close to a sphericity of 0.95 and the second is around 0.8. Many nodules are almost spherical, i.e. with a mean sphericity of 0.93 and a standard deviation of 0.09. In CGI, a high level of sphericity with a peak close to 0.95 is noticed but the frequency is half that of SGI at this latter value. The mean sphericity value is 0.72 $\pm$ 0.23 and below 0.9, frequency stays constant until 0.4. Therefore, in CGI, nodules with a high level of sphericity are present but also vermicules with an occurrence frequency which is constant below a sphericity of 0.8. Figure 6 shows graphite particles in CGI at different levels of sphericity. For sphericities below 0.8, vermicules are noticed while beyond this value, more or less spherical nodules are observed. Thus a sphericity of 0.8 can be employed to separate nodules and vermicules. Although it is a subjective threshold, it allows measuring particles size.

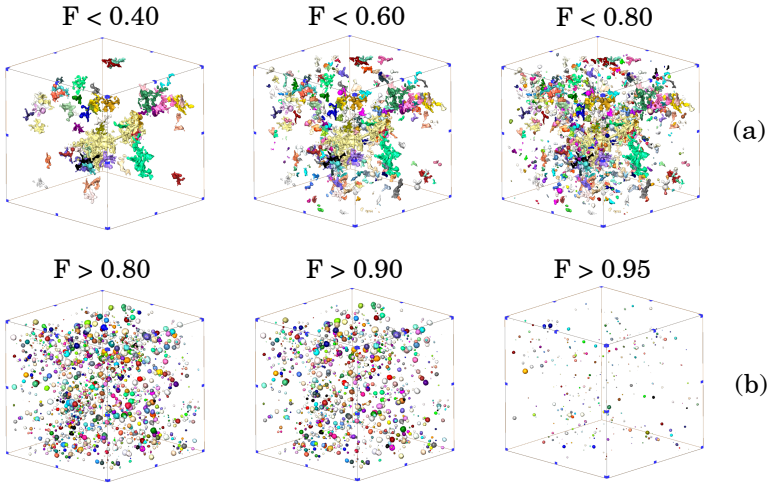

Figure 6: Rendering of graphite particles at different levels of sphericity in CGI: vermicules (a) and nodules (b).

3.1.2. Size characterizations

In order to assess graphite morphology, the 3D equivalent diameter and Feret diameters are employed for respectively nodules and vermicules. Indeed, Feret diameter, as a measurement of spatial spread, is more appropriate for graphite vermicules. For spherical nodules, the 3D equivalent diameter seems to be the most pertinent parameter. For SGI, the distribution is well spread from around 8 to 50 μm with a mean value of 26 $\pm$ 7 μm. For CGI, many small elements must be present because of the truncation for diameters less than 5 μm (all volumes less than 2x2x2 voxels are neglected). The mean value for the vermicular graphite cast iron reaches 19 $\pm$ 8 μm.

For vermicules characterization, minimum and maximum Feret diameters were used. Whether for the maximum or the minimum diameters, results spread from around 15 to 225 μm and from 15 to 120 μm respectively. The mean maximum Feret diameter reaches 64 $\pm$ 35 μm while the average minimum Feret diameter is twice less than the maximum one. The Feret shape factor, which corresponds to the ratio of extreme Feret diameters, underlines a moderate shape anisotropy with a mean value close to 0.5.

Finally, thickness of graphite vermicules was measured using granulometry by opening, i.e. a succession of erosion and dilatation, with ImageJ software. A thickness close to 10 μm is obtained for 50% of analysed elements.

3.1.3. Differences between core and surface of foundry bars

Some measurements were also achieved on the surface of foundry bars in order to ascertain potential microstructural gradients. For CGI, some fluctuations are noticed. Indeed, at the surface, the graphite volume fraction is lower of around 1 %. In terms of graphite shape, vermicules are notably similar while nodules are larger close to the surface. The same trend is observed for SGI although to a lesser extent. Therefore, the fatigue specimens are extracted from the core of the bars where the microstructure was more homogeneous.

3.2. Monotonic behaviour

To assess possible differences in monotonic behaviour between SGI and CGI, tensile and micro/macro Vickers hardness tests were performed.

3.2.1. Hardness results

Macro-hardness values are close between spheroidal and vermicular graphite cast irons. Indeed, a mean value of 253 ± 11 HV was measured for the SGI and 222 ± 10 HV for the CGI. In addition to graphite, shrinkages pores and the matrix nature conduct to hardness fluctuations due to possible variations on the elements located below the indentations. For micro-hardness measurement carried out on the matrix of cast irons, a higher value was assessed for CGI with a mean value of 321 ± 36 Vickers than for SGI with 247 ± 35 HV. The volume fractions being sensibly identical (14.5% for SGI and 15.7% for CGI), there is *a priori* no effect of the graphite quantity on mechanical responses.

3.2.2. Tensile tests results

The ultimate tensile strength, yield strength and elastic modulus were determined from four tensile tests for the SGI and five for the CGI (Fig. 7).

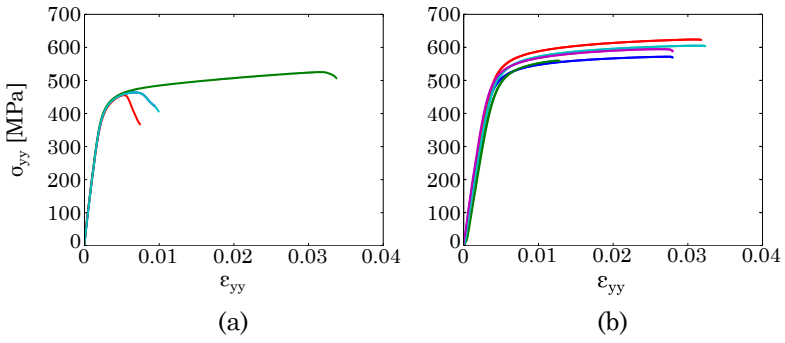

Figure 7: Tensile curves for the spheroidal (a) and the compacted (b) graphite cast irons.

The SGI has a larger Young's modulus (177 GPa) than CGI (140 GPa). The yield strength $\sigma_{0.2}$ and ultimate tensile strength σ_m of the CGI are almost 100 MPa higher than that measured for the SGI. Indeed, the yield strengths

are 451 ± 3 and 529 ± 13 MPa while the ultimate strengths are 475 ± 35 and 593 ± 23 MPa for SGI and CGI, respectively. These results are in line with micro-hardness tests results.

Elongations to failure $A\%$ are generally greater for the CGI than for the SGI with respectively mean values of 2.7 and 1.6 %. These latter depend on the microstructural constituents and nature of the matrix, but here particularly on the shrinkage pores presence. On specimens' surfaces, no defects were noticed. However, X-ray microtomography highlighted internal defects in large samples of SGI with some micro shrinkage cavities that may reach up to around 250x350x50 μm^3 in size (Fig. 8).

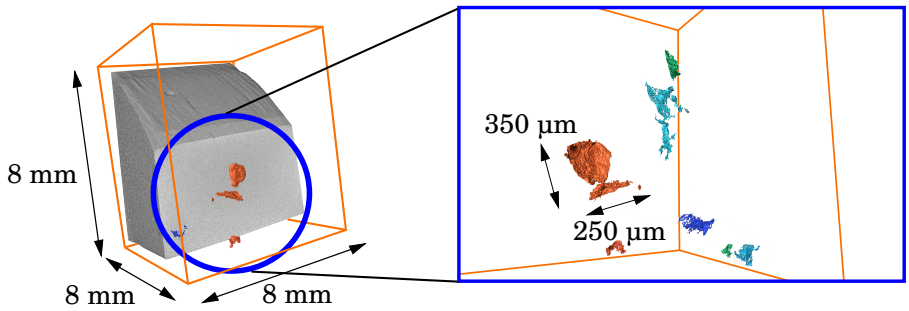

Figure 8: Some shrinkage porosities revealed by microtomography in SGI close to the foundry bar surface (1 voxel = 12.3 μm).

These defects in SGI may lead to low values of elongation to failure with a large dispersion. Therefore, it is difficult to conclude on the influence of the cast iron type or graphite shape as respect to this property.

3.3. Fatigue crack growth behaviour

Graphite cast irons are used in many fatigue applications and especially in a life range from 10^2 to 10^6 cycles. Due to presence of defects or graphite particles, crack is suspected to initiate very early in the lifetime. To preserve this latter, design approach considering fatigue crack propagation analysis is of major interest and justify the study of long crack propagation behaviour. Therefore, only this aspect is studied here.

3.3.1. Paris' curves

Although, fatigue propagation tests were carried out at a smaller maximum load for CGI, an earlier crack initiation was noticed, i.e. around 65,000 cycles for CGI as compared to about 85,000 cycles for SGI. Then, fatigue crack propagates longer in CGI until 350,000 cycles against 200,000 cycles in SGI.

As a reminder, the range of stress intensity factor ΔK_I and the crack length a were computed by the projective approach based on DIC and Williams' model (Section 2.3.3). Figure 9 (a) shows the relationship between the experimental fatigue crack length and the cycles number after the pre-cracking step. The evolution of the crack length, i.e. the crack tip position along the horizontal direction, with the number of cycles was fitted with polynomial curves before computing the crack growth rate for the purpose of reducing noise. The crack growth rates da/dN are plotted against the stress intensity factor range ΔK_I in Figure 9 (b).

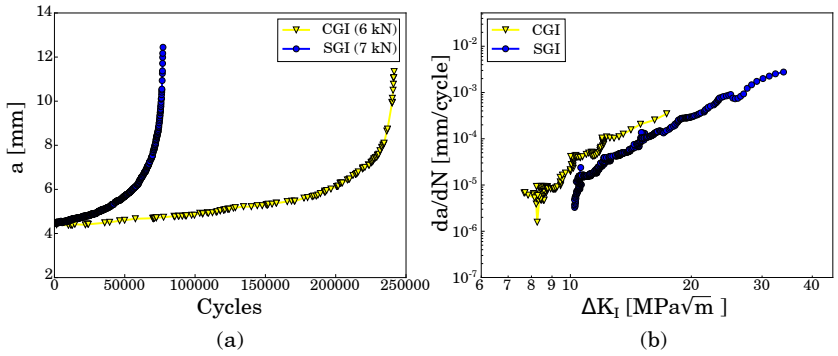

Figure 9: Crack length versus cycles (a) and da/dN - ΔK_I (b) curves for the two studied cast irons.

The measured Paris' coefficients C are close between the two cast irons with $10^{-9.77}$ and $10^{-10.74}$ for SGI and CGI respectively. The slope m is slightly higher for CGI, i.e. close to 6.09 versus 4.82 for SGI, conducting to a faster crack propagation. SGI's SIF range ΔK_I at the unstable failure, i.e. the vertical asymptote to the propagation curve, is higher than that of CGI with respectively 35 and

20 MPa$\sqrt{\text{m}}$.

For the low crack velocity zone of Fig. 9 (b), 'knees' are noticed on the range 10^{-4} to 10^{-7} mm per cycle unlike in some flake graphite cast irons [20]. This phenomenon can be interpreted by a proximity to a crack propagation threshold, which is around 10 MPa$\sqrt{\text{m}}$ for SGI and 8 MPa$\sqrt{\text{m}}$ for CGI. Thus, a fatigue crack propagates for a lower SIF value in the compacted graphite cast iron. Nonetheless, the so-obtained thresholds are probably inaccurate. Indeed a more precise measurement could be carried out with a ΔK_I-decreasing crack propagation test [32].

To compare the crack propagation rates conveniently, crack propagation rate was plotted as a function of the stress intensity factor range ΔK_I divided by the Young's modulus E such as suggested by Ogawa *et al.* [21]. Figure 10 shows the result of this normalization where the elastic moduli correspond to 177 GPa for SGI and 140 GPa for CGI.

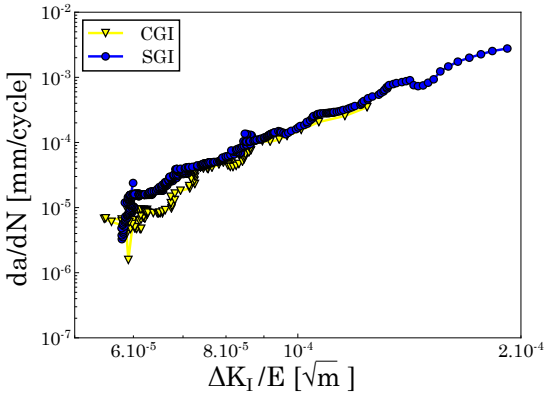

Figure 10: Crack propagation rates as a function of SIF range ΔK_I divided by Young's modulus E.

Normalization leads to an overlap of the two propagation curves. The Young's modulus ratio allows accounting for most of the gap between CGI and SGI in the Paris' regime. Young's modulus is representative of the graphite volume fraction and its morphology. Nonetheless, as it was specified before,

the graphite volume fractions are sensibly identical for the two cast iron grades (as discussed in Section 3.2.1), thus herein Young's modulus depends mainly on graphite shape and especially on the sphericity as stated by [38].

3.3.2. Fractography

Fatigue fracture surfaces of the two cast irons were examined with scanning electron microscopy (Fig. 11). For both cast irons, the dominating failure mode is ductile striated crack growth, together with isolated facets of cleavage that occur close to graphite particles in the matrix. Larger transgranular cleavage facets highlight the brittleness of CGI. This pairing of striation and cleavage planes that go into tear rivers, oriented in all directions, is known as 'Quasi Cleavage' [39] and occurs in both cast irons.

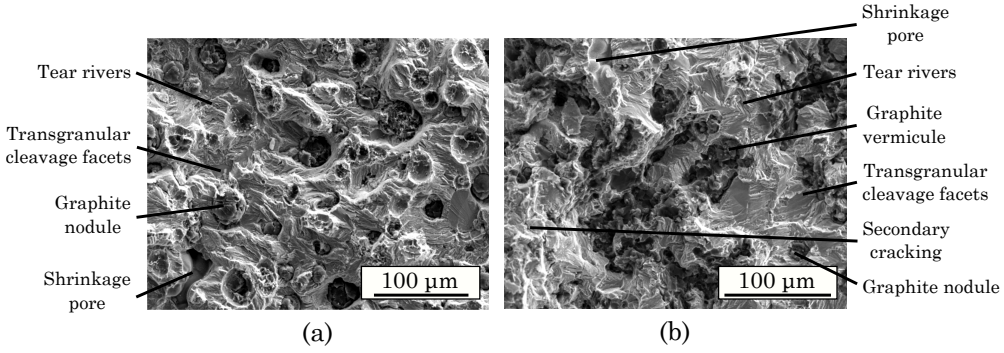

Figure 11: Fracture surfaces of SENT specimens for SGI (a) and CGI (b).

The graphite surface fractions on the crack paths were 21% and 27% for SGI and CGI (with the majority of the particles observed consisting of degenerated nodules and vermicules for CGI) respectively. These values are higher than the graphite volume fractions in the bulk close to 15%. This difference highlights that crack is attracted by graphite particles especially in CGI. Furthermore, for CGI, a secondary cracking is noticed on the fracture surfaces.

3.3.3. Crack paths

X-ray microtomography was also employed to investigate crack paths; the test conditions are the same as for the graphite characterization (section 2.2). Macroscopic SENT specimens, having the geometry shown in Fig. 4 (b), were fatigue pre-cracked. In order to obtain appropriate specimens for the microtomography, i.e. to get a sufficient resolution, *in situ* specimens with a 2.2x2.2 mm^2 cross-section were cut by electro discharge machining inside the SENT macroscopic specimens. Moreover, as tomographic specimens have to present a fatigue crack while maintaining a confined plasticity, macro-specimens were loaded with a stress intensity factor range close to crack thresholds, i.e. with a maximum value of 12 MPa$\sqrt{m}$ for SGI and 10 MPa$\sqrt{m}$ for CGI. Therefore, plasticity was confined at crack tips with lower plastic zone radii of 250 μm in plane stress case [40]. Fatigue cycling was stopped when cracks had sufficiently propagated, i.e. close to 7 mm, in order to extract *in situ* specimens for tomography (Fig. 12).

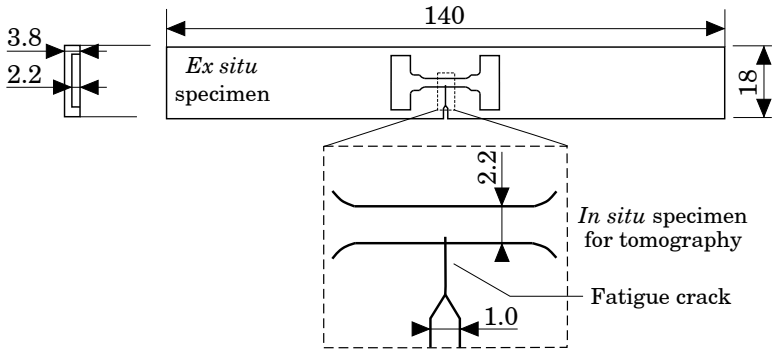

Figure 12: Extraction principle of the specimen *in situ* in the *ex situ* fatigue test piece (dimensions in mm).

A three-dimensional rendering of cracks (Fig. 13) was obtained by thresholding the 3D images with a region growing approach [41]. For graphite cast irons, grey levels of crack and graphite are close, thus all the nodules and vermicules connected to the crack are included in the crack path. For the CGI's crack, a perfect planar propagation is observed especially in the (y,z) plane and the

two last representations show limited bifurcations. SGI's crack front presents a certain curvature with the shortest crack length on the *ex situ* specimen surface (the specimen extraction was not carried out over the entire thickness of the macroscopic test piece). This latter part corresponds to the plane stress condition of the *ex situ* test piece while the longer crack side corresponds to the plane strain case.

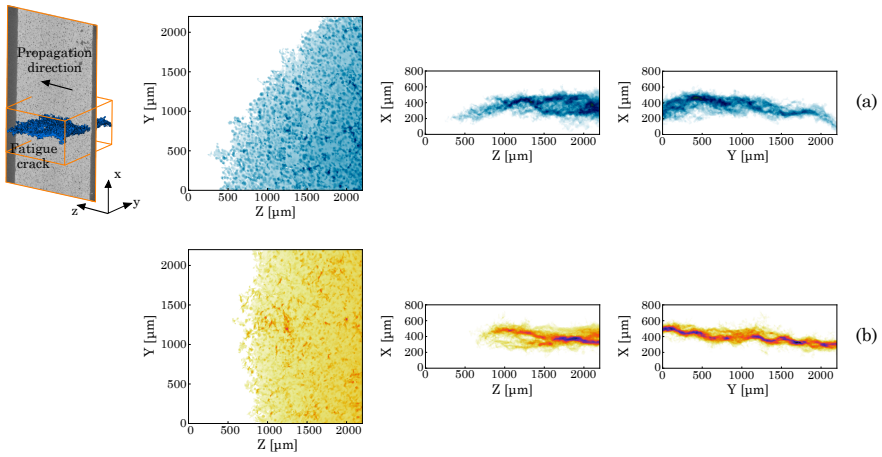

Figure 13: 3D cracks observed from microtomography in the three main planes for SGI (a) and CGI (b).

After *in situ* crack opening tests, the specimens were broken in tension to conduct complementary analysis at a higher resolution (voxel size = 1.9 μm). The broken specimens were scanned with X-ray microtomography and aligned with 3D reference image of *in situ* tensile tests (Fig. 14). In central part of specimens, this gives a good overview of the crack, i.e. a good coincidence with cracks obtained from Digital Volume Correlation (DVC) [42] residues, and of their paths through graphite particles. The DVC computation was carried out between the 3D images taken at the reference state and at a load of 450 N.

Previously, a crucial role of graphite in the crack propagation process was shown by the high graphite fraction in the fracture surface. It is apparent that cracks jump from one graphite particle to the neighbouring one. For spheroidal graphite, ferrite-nodule interfaces debonding was the most prevalent damage

mechanism as confirmed by fracture surfaces analysis (Fig. 11 (b)) while for compacted graphite, phenomena are less obvious. Indeed, Figure 14 highlights damage with internal cracking of graphite as stated by [43] and some ferrite-vermicule interfaces debondings. The orientation of the graphite with respect to the direction of maximum stress seems to influence the crack propagation mechanism. Indeed, graphite particles perpendicular to the loading direction appear to undergo debonding while those oriented in the direction of force are broken.

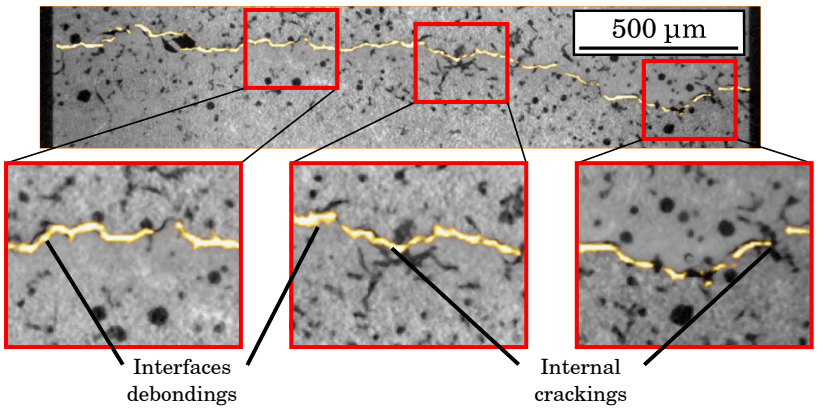

Figure 14: Fracture of graphite particles in CGI highlighted by microtomography ((x,y) plane at Z = 1100 μm). The crack, shown in yellow, corresponds to the residue of a DVC computation.

3.3.4. Roughness of crack paths

Finally, roughness measurement was carried out by means of an interferometric optical profilometer VEECO Wyko NT1100 at a resolution of 640x480 pixels, using the stitching mode to extend the studied area. The vertical resolution enables to reach *a priori* 3 Angström. Results are shown in Fig. 15 where similar roughness scales were used to enable a direct comparison between cast irons. Crack tip positions were superimposed on the roughness maps to visualize the possible correlation between crack growth and roughness.

Locations of the crack fronts are extracted by direct image analysis of the 3D

reconstructed data because the crack tip is visible under the maximum load when the crack is fully open. Using a Python script, the voxel at the crack tip was manually selected in each slice (x, z) plane containing the loading direction and perpendicular to the crack front (the landmark is specified in Fig. 13) and coordinates were recorded. In the vicinity of the crack fronts, for both cast irons, the roughness fluctuates significantly. The propagation of the fatigue crack in the case of CGI occurs relatively uniformly in thickness, unlike SGI. On the crack propagation zones, standard deviations of roughness were determined. Values in the order of magnitude of the typical size of graphite particles were measured with 52.3 μm and 31.4 μm for SGI and CGI respectively. However, a few shrinkages pores (even in the case of CGI, which did not appear to have any during the tomographic analysis) were observed and should have an impact on the obtained values.

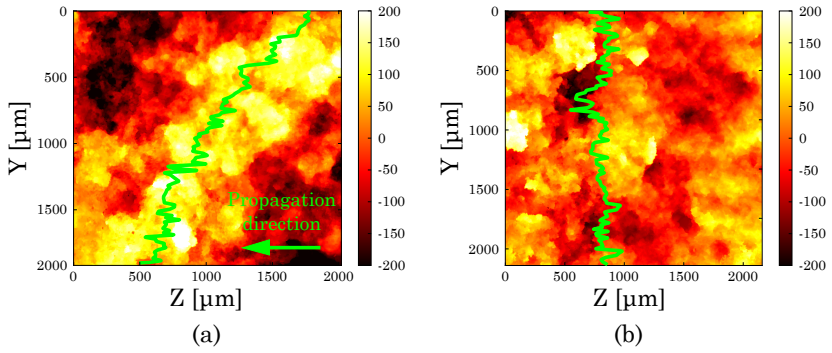

Figure 15: Roughness maps (μm) for SGI (a) and CGI (b) with crack front locations.

3.4. Discussion

In terms of crack propagation, spheroidal graphite cast iron presents better mechanical properties considering the higher stress intensity factors at the threshold and at the failure than those of CGI. For a same crack length, a higher loading is necessary to propagate the crack and to conduct to failure. By comparing cast irons with different matrices and vermicular graphite percentage, Lee and Chang [44] observed that the m coefficient of Paris' law increases with

an increase in vermicularity and the effect of this latter is more pronounced than the effect of the ferritic or pearlitic matrix type. On the opposite, toughness depends first on the matrix and then on vermicularity. Furthermore, normalizing by the Young's modulus, that varies linearly with nodularity [38] and therefore with the morphology of graphite, enables the two cast irons to lie on the same scatter band in the propagation regime and near the crack threshold. Graphite volume fractions are sensibly similar between the two cast irons, i.e. around 15 %, and are in agreement with standards in grey cast irons [6]. The difference in propagation behaviour between the two cast irons is therefore based *a priori* on the geometry of graphite particles. However, the difference in K_c remains and can be explained by a higher mechanical strength and therefore a reduced toughness of the compacted graphite cast iron, a property that can be affected by the shape of the vermicules, but also by the brittleness and non linear effects of the matrix as mentioned in [44]. Indeed, monotonic properties are higher for CGI than SGI especially in terms of yield and ultimate strengths. Micro-hardnesses are also higher for the vermicular graphite cast iron. Alloying elements must contribute to the difference in mechanical behaviour between the two cast irons. In CGI, there are silicon and molybdenum as for the SGI, but also nickel. Besides the silicon content is more important in compacted graphite cast iron (Tab. 1). Allafi *et al.* [45] studied the influence of a silicon content ranging from 2.1 to 3.3 % on the microstructure of a spheroidal graphite cast iron. They have shown that by increasing its content, the nodules number increases and the volume of the shrinkage pores decreases. In [46], silicon effects on the maximum tensile strength, elongation and toughness have been highlighted for a SGI. It causes the increase of mechanical resistance and a decrease of ductility as well as the failure energy. Therefore, the higher strength of compacted graphite cast iron may be due, on the one hand, to a composition richer in Si and Ni and therefore a stronger matrix and this could explain the higher micro-hardness, but also, on the other hand, to a better cohesion between graphite vermicules and the matrix [47].

A graphite morphology analysis was carried out with X-ray microtomography. In the spheroidal graphite cast iron, the geometry of graphite consists mostly in nodules close to spheres with a sphericity beyond 0.9. Moreover, graphite nodules show a moderate size with a mean diameter around 25 μm. In the compacted graphite cast iron, half the volume fraction of the graphite particles are highly connected vermicules. They seem to present a certain anisotropy with a Feret shape factor of 0.5 and mean maximum and minimum Feret diameters of respectively 65 μm and 31 μm. Nodules constitute the other half of the population of graphite elements in CGI. Like in SGI, nodules are close to spheres with a sphericity around 0.9, but they are smaller in the compacted graphite cast iron with a mean equivalent diameter of 20 μm. Furthermore, a more important proportion of nodules is noted close to the surface of cast bars. As shown by Dawson *et al.* [23], nodularity increases with the cooling rate so that this could explain higher nodules proportions in the periphery of the foundry bar that solidifies at faster cooling rate than the centre. This phenomenon could have an impact on a cast part. In spheroidal graphite cast iron, some irregular and degenerated graphite gathering multiple nodules (and shrinkage pores) were noticed, that could conduct to an early crack initiation [48]. For compacted graphite cast iron, defects are more difficult to detect in microtomography because of the relatively close grey levels between air of pores and graphite coupled with similar complex geometry between micro shrinkages and vermicules.

Graphite is an important microstructural constituent in grey cast irons, which plays a key role in the material performance. Indeed, the high sphericity of the nodules for both SGI and CGI contribute to obtaining relatively high crack growth thresholds [49]. While, the moderate dimensions of graphite lead to moderate fracture surface roughness [50]. Benedetti *et al.* have estimated opening stress intensity factors that increase with roughness in ferritic ductile cast iron. The roughness is slightly smaller for compacted graphite cast iron (31.4 μm) than for spheroidal graphite cast iron (52.3 μm). Thus, Roughness

Induced Crack Closure (RICC) must be more important for SGI. Another physical origin of crack closure effects is crack-tip plasticity. Curved crack front was noticed with microtomography for the SGI unlike the CGI. For the spheroidal graphite cast iron, the plastic zone size at the crack front is likely to increase rapidly due to its smaller yield strength, especially on the short crack side in plane stress, and the confined plasticity condition may even be violated at the crack front. A large plastic zone at the surface may result in a stronger Plasticity Induced Crack Closure (PICC) effect, hence a more curved crack front. Consequently, RICC but also PICC could explain a shift between Paris' curves of SGI and CGI.

CGI has the highest crack growth rate da/dN compared to SGI because the large aspect ratio of compacted graphite must enable cracks to move easier through graphite. Indeed, the graphite surface fraction on the fracture surface is higher in the case of the CGI than SGI. In addition, the standard deviation of the roughness is lower for the CGI. Therefore, the crack propagates easier, i.e. with less bifurcation, in the case of vermicular graphite particles. Analysis of the fracture surfaces of the fatigue specimens reveals that in the SGI spheroid debonding does not involve systematically a complete nodule detachment. It is usually total for graphite spheroids and less obvious for the least spherical particles and especially degenerated graphite. For the CGI, the complex graphite morphology, together with the rounded edges and rough surfaces, results in strong adhesion between the graphite and the iron matrix. The graphite–matrix interface is extremely irregular, with some sharp corners, high stress concentrators that in some cases constitute imminent microcracks that emanate from the vermicules. Furthermore, the distribution of graphite particles appears to be important in the propagation of the fatigue crack. The orientation of the graphite with respect to the direction of maximum stress will influence the propagation mechanism of the crack in the vicinity of graphite particles. Indeed, graphite particles parallel to the loading direction are broken while those oriented perpendicular to the loading axis seem more likely to debond.

The better resistance to crack propagation of spheroidal graphite cast iron may be due to more frequent decelerations because of the shape of the nodules that blunt the crack [51], this effect would be all the greater at low propagation velocities. Vermicules, on the other hand, have an elongated shape and anisotropic behaviour that favour a stress concentration effect on the matrix between two vermicules tips, more important than for spheroids [47, 51]. This would result in lower resistance to microcrack initiation, and probably a lower blunting effect of existing cracks. The fracture surfaces confirm that graphite particles do not facilitate debonding in the same way as lamellae in flake graphite cast iron [23, 52]. CGI presents mechanical properties that are between spheroidal and Flake Graphite cast Irons with a thermal conductivity that is better than SGI [9]. Thus, compacted graphite cast iron could constitute a material of choice for structures working at high temperature such as exhaust systems.

4. Conclusion

The graphite shape plays an important role in the mechanical and physical properties of cast irons. In this work, fatigue tests and 3D characterisations of the graphite with microtomography were conducted for spheroidal and compacted graphite cast irons. Main results obtained are as follows:

- A parameter calculated by dividing the stress intensity factor range by the Young's modulus constitutes an effective mean of correlating for the crack propagation rate in the Paris' regime and near crack thresholds for the two studied cast irons. The difference in K_c remains and can be explained by a higher mechanical strength and thus a reduced toughness of CGI, a property that can be affected by the stress concentration effect of the vermicules, but also by the brittleness of the matrix.

- The crack propagation rate was larger in CGI than in SGI. It is obvious that the graphite shape influences the fatigue crack propagation rate; it

must be of the first order, but the behaviour of the matrix must also be significant. In the case of compacted graphite cast iron, the proportion of graphite on the fracture surface is higher and the roughness is more limited. Furthermore, the graphite orientation in relation to the maximum stress direction appears to affect the crack propagation mechanism close to graphite particles. Graphite fracture seems to be the main mode of fatigue crack propagation. In some cases, crack propagates over length equal to the vermicule size after the matrix/graphite interfaces debonding, but certainly in a lesser extent than for flake graphite cast iron.

Finally, one of the prospects of this work could be to study cast irons with different percentages of vermicules/nodules to validate normalization by Young's modulus and to propose an analytical formula for ΔK_{th} or K_{op}. This would be in combination with the detailed analysis of graphite morphology already initiated here.

5. Acknowledgements

The ISIS4D X-Ray CT platform has been funded by International Campus on Safety and Intermodality in Transportation (CISIT), the Nord-Pas-de-Calais Region, the European Community and the National Center for Scientific Research. The ELSAT2020 project is co-financed by the European Union with the European Regional Development Fund, the French state and the Hauts-de-France Region Council. The authors gratefully acknowledge the support of these institutions.

The authors wish to thank Groupe PSA for providing materials. Corentin Martel, François Lesaffre, Matthieu Meersdam and Bruno Haubreux (LaMcube, France) are also acknowledged for help in mechanical tests and microstructures characterizations.

References

[1] E Charkaluk, A Bignonnet, A Constantinescu, and K Dang Van. Fatigue design of structures under thermomechanical loadings. *Fatigue & Fracture of Engineering Materials & Structures*, 25(12):1199–1206, 2002.

[2] F Szmytka, P Michaud, L Rémy, and A Köster. Thermo-mechanical fatigue resistance characterization and materials ranking from heat-flux-controlled tests. Application to cast-irons for automotive exhaust part. *International Journal of Fatigue*, 55:136–146, 2013.

[3] B Miao, N Wood, W Bian, K Fang, and MH Fan. Structure and growth of platelets in graphite spherulites in cast iron. *Journal of Materials Science*, 29(1):255–261, 1994.

[4] N Llorca-Isern, J Tartera, M Espanol, M Marsal, G Bertran, and S Castel. Internal features of graphite in cast irons. Confocal microscopy: useful tool for graphite growth imaging. *Micron*, 33(4):357–364, 2002.

[5] G Hütter, L Zybell, and M Kuna. Micromechanical modeling of crack propagation in nodular cast iron with competing ductile and cleavage failure. *Engineering Fracture Mechanics*, 147:388–397, 2015.

[6] M Shikida, M Sakane, and M Ohnami. Fatigue crack propagation for cast iron rotating disk. *JSME international journal. Ser. A, Mechanics and material engineering*, 38(1):104–110, 1995.

[7] L Augustins, F Hild, R Billardon, and S Boudevin. Experimental and numerical analysis of thermal striping in automotive brake discs. *Fatigue & Fracture of Engineering Materials & Structures*, 40(2):267–276, 2017.

[8] J Tartera, N Llorca-lsern, M Marsal, and JL Rojas. Similarities of nucleation and growth of spheroidal and compacted graphite. *International Journal of Cast Metals Research*, 16(1-3):131–135, 2003.

[9] J Le Gal. *Techniques de l'Ingénieur - Les fontes à graphite vermiculaire*. 2014.

[10] BI Imasogie and U Wendt. Characterization of graphite particle shape in spheroidal graphite iron using a computer-based image analyzer. *Journal of Minerals and Materials Characterization and Engineering*, 3(01):1–12, 2004.

[11] J Li, L Lu, and MO Lai. Quantitative analysis of the irregularity of graphite nodules in cast iron. *Materials Characterization*, 45(2):83–88, 2000.

[12] HT Angus. *Cast iron: physical and engineering properties*. Elsevier, 2013.

[13] GL Greno, JL Otegui, and RE Boeri. Mechanisms of fatigue crack growth in austempered ductile iron. *International Journal of Fatigue*, 21(1):35–43, 1999.

[14] M Lampic. A new opportunity for cast iron with compacted graphite. *Giesserei*, 79:871–878, 1992.

[15] C Verdu, J Adrien, and JY Buffière. Three-dimensional shape of the early stages of fatigue cracks nucleated in nodular cast iron. *Materials Science and Engineering: A*, 483:402–405, 2008.

[16] C Labrecque and M Gagne. Interpretation of cooling curves of cast irons: A literature review. In *One Hundred Second Annual Meeting of the American Foundrymen's Society*, pages 83–90, 1998.

[17] P Clement, J Pl Angeli, and A Pineau. Short crack behaviour in nodular cast iron. *Fatigue & Fracture of Engineering Materials & Structures*, 7(4):251–265, 1984.

[18] C Guillemer-Neel, V Bobet, and M Clavel. Cyclic deformation behaviour and bauschinger effect in ductile cast iron. *Materials Science and Engineering: A*, 272(2):431–442, 1999.

[19] B Stokes, N Gao, and PAS Reed. Effects of graphite nodules on crack growth behaviour of austempered ductile iron. *Materials Science and Engineering: A*, 445:374–385, 2007.

[20] MN James and L Wenfong. Fatigue crack growth in austempered ductile and grey cast irons—stress ratio effects in air and mine water. *Materials Science and Engineering: A*, 265(1-2):129–139, 1999.

[21] T Ogawa and H Kobayashi. Near-threshold fatigue crack growth and crack closure in a nodular cast iron. *Fatigue & Fracture of Engineering Materials & Structures*, 10(4):273–280, 1987.

[22] JR Davis. Classification and basic metallurgy of cast irons. *American Society of Metals. ASM specialty handbook cast iron. Illinois: ASTM*, pages 4–17, 1996.

[23] S Dawson. Compacted graphite iron: mechanical and physical properties for engine design. *SinterCast Technical Publication*, 1999.

[24] ICH Hughes and J Powell. Compacted graphite irons-high quality engineering materials in the cast iron family. *SAE transactions*, pages 1–15, 1984.

[25] JC Pina, S Shafqat, VG Kouznetsova, JPM Hoefnagels, and MGD Geers. Microstructural study of the mechanical response of compacted graphite iron: An experimental and numerical approach. *Materials Science and Engineering: A*, 658:439–449, 2016.

[26] DM Stefanescu. Solidification of eutectic alloys: Cast iron. *ASM Handbook.*, 15:168–181, 1988.

[27] P Bastid. *Comportement thermomécanique de fontes à graphite sphéroïdal pour collecteurs d'échappement.* PhD thesis, École Nationale Supérieure des Mines de Paris, 1995.

[28] N Limodin, T Rougelot, and J Hosdez. ISIS4D - In Situ Innovative Set-ups under x-ray microtomography. `http://isis4d.univ-lille1.fr/`, 2013.

[29] AC Kak, M Slaney, and G Wang. Principles of computerized tomographic imaging. *Medical Physics*, 29(1):107–107, 2002.

[30] ZIB (Konrad-Zuse-Zentrum für Informationstechnik Berlin) and VSG (Visualization Sciences Group). Avizo Online Help. `http://www.fei.com/software/avizo-3d-resources/`, 2012.

[31] J Schindelin, I Arganda-Carreras, E Frise, V Kaynig, M Longair, T Pietzsch, S Preibisch, C Rueden, S Saalfeld, B Schmid, et al. Fiji: an open-source platform for biological-image analysis. *Nature methods*, 9(7):676, 2012.

[32] R Gangloff, D Slavik, R Piascik, and R Van Stone. Direct current electrical potential measurement of the growth of small cracks. In *Small-Crack Test Methods*. ASTM International, 1992.

[33] J Hosdez, JF Witz, C Martel, N Limodin, D Najjar, E Charkaluk, P Osmond, and F Szmytka. Fatigue crack growth law identification by digital image correlation and electrical potential method for ductile cast iron. *Engineering Fracture Mechanics*, 182:577–594, 2017.

[34] R Seghir, JF Witz, and S Courdert. YaDICs Digital image correlation 2/3D software. `http://yadics.univ-lille1.fr/`, 2014.

[35] R Hamam, F Hild, and S Roux. Stress intensity factor gauging by digital image correlation: Application in cyclic fatigue. *Strain*, 43(3):181–192, 2007.

[36] J Hosdez, M Langlois, JF Witz, N Limodin, D Najjar, E Charkaluk, P Osmond, A Forre, and F Szmytka. Plastic zone evolution during fatigue crack growth: Digital image correlation coupled with finite elements method. *International Journal of Solids and Structures*, 171:92–102, 2019.

[37] ML Williams. The bending stress distribution at the base of a stationary crack. *Journal of Applied Mechanics*, 28(1):78–82, 1961.

[38] T Sjögren. *Influences of the graphite phase on elastic and plastic deformation behaviour of cast irons*. PhD thesis, Institutionen för ekonomisk och industriell utveckling, 2007.

[39] JM Kendal, MN James, and JF Knott. The behaviour of physically short fatigue cracks in steels. In *The behaviour of short fatigue cracks*, volume 1, pages 241–258. Mechanical Engineering Publications, 1986.

[40] D Broek. *Elementary engineering fracture mechanics*. Springer Science & Business Media, 2012.

[41] P Soille. *Morphological image analysis: principles and applications*. Springer Science & Business Media, 2013.

[42] N Dahdah, N Limodin, A El Bartali, J-F Witz, R Seghir, E Charkaluk, and J-Y Buffiere. Damage investigation in a319 aluminium alloy by x-ray tomography and digital volume correlation during in situ high-temperature fatigue tests. *Strain*, 52(4):324–335, 2016.

[43] H Pirgazi, S Ghodrat, and L Kestens. Three-dimensional EBSD characterization of thermo-mechanical fatigue crack morphology in compacted graphite iron. *Materials Characterization*, 90:13–20, 2014.

[44] SC Lee and YBn Chang. Fracture toughness and crack growth rate of ferritic and pearlitic compacted graphite cast irons at 25°c and 150°c. *Metallurgical Transactions A*, 22(11):2645–2653, 1991.

[45] J Khalil-Allafi and B Amin-Ahmadi. Effect of mold hardness on microstructure and contraction porosity in ductile cast iron. *Journal of Iron and Steel Research, International*, 18(4):4467–47, 2011.

[46] A Alhussein, M Risbet, J Favergeon, D Balloy, P Royes, JC Tissier, A Bastien, JP Chobaut, B Lepolard, and P Dufey. Evolution des pro-

prietes mecaniques et de la microstructure de fonte GS ferritique vis-a-vis de la teneur en silicium. *Fonderie Magazine*, 60:21–27, 2015.

[47] WM Mohammed, E Ng, and MA Elbestawi. On stress propagation and fracture in compacted graphite iron. *The International Journal of Advanced Manufacturing Technology*, 56(1-4):233–244, 2011.

[48] T Palin-Luc, S Lasserre, and Y Berard. Experimental investigation on the significance of the conventional endurance limit of a spheroidal graphite cast iron. *Fatigue & Fracture of Engineering Materials & Structures*, 21(2):191–200, 1998.

[49] P Hübner, H Schlosser, G Pusch, and H Biermann. Load history effects in ductile cast iron for wind turbine components. *International Journal of Fatigue*, 29(9-11):1788–1796, 2007.

[50] M Benedetti, V Fontanari, and D Lusuardi. Effect of graphite morphology on the fatigue and fracture resistance of ferritic ductile cast iron. *Engineering Fracture Mechanics*, 206:427–441, 2019.

[51] G Pusch, S Henkel, H Biermann, P Hübner, A Ludwig, P Trubitz, T Mottitschka, and L Krüger. Determination of fracture mechanics parameters for cast iron materials under static, dynamic and cyclic loading. In *Recent trends in fracture and damage mechanics*, pages 159–196. Springer, 2016.

[52] H Germann, P Starke, and D Eifler. Resistivity-based evaluation of the fatigue behavior of cast irons. *Metallurgical and Materials Transactions A*, 43(8):2792–2798, 2012.